

Cite this: DOI: 00.0000/xxxxxxxxxx

# Bouncing-to-wetting transition for droplet impact on soft solids

Surjyasish Mitra <sup>a</sup>, Quoc Vo <sup>b,\*</sup>, and Tuan Tran <sup>b,\*\*</sup>

Received Date  
Accepted Date

DOI: 00.0000/xxxxxxxxxx

Soft surfaces impacted by liquid drops trap more air than their rigid counterpart. Due to the extended lifetime of this air film, the dynamics and eventual rupture of trapped air film depend on its interaction with the air cavity developed in the liquid during impact. In this work, we investigate the interaction between air cavity collapse and air film rupture for drops impacting on soft, hydrophobic surfaces using high-speed laser interferometry. We first reveal three different rupture dynamics of the trapped air film; the rupture may initiate either at the center of the dimple, at the edge of the dimple or at a random point in the dimple's outer rim. We found that the transition between these rupture dynamics depends on both the impact velocity and the surface elasticity. Further, in the most special case of air-film rupture, the so-called dimple inversion, the rupture is directly caused by the collapsing air cavity in the droplet bulk. We further observe that in such cases, high-speed jets occur. We then provide a detailed characterization of the collapsing dynamics of the air cavity and subsequent jetting.

## 1 Introduction

The air film separating an impacting liquid droplet with an impacted surface plays a crucial role in dictating impact outcomes. For high velocity impacts, reducing the pressure of this air film leads to splash suppression<sup>1</sup>, a crucial goal in printing technology<sup>2</sup>. For low velocity impacts, the presence of a sustained air film leads to droplet bouncing<sup>3–7</sup>, a phenomenon that forms the basis of self cleaning applications<sup>8</sup>. As a result, numerous investigations have been focusing on impact phenomena involving the intervening air film right at the moment wetting occurs<sup>1,3–7,9</sup>.

Typically, the prelude to the final touchdown between an approaching droplet and a solid surface is the formation of a thin air film in which lubrication pressure is built up. The lubrication pressure subsequently becomes sufficiently large that it deforms the droplet's bottom surface, creating a central dimple surrounded by an outer edge with one or two kinks, the regions where the air film thickness is minimum<sup>5,6,10</sup>. For impact on hydrophilic surfaces, bouncing is ensured at low impact velocity. For higher impact velocity, the air film typically ruptures either at inner or outer kink leading to wetting initiation<sup>5,6</sup>. Most droplets impacting smooth hydrophilic surfaces like glass or mica either bounce or deposit due to random wetting initiation.

Impact outcomes on hydrophobic surfaces are markedly different<sup>11,12</sup>. An impacting droplet, above a critical impact velocity,

may develop a pyramidal structure due to capillary waves induced upon impact. This in turn leads to formation of a cylindrical air cavity that penetrates deeply into the droplet and eventually collapses, shooting out a liquid jet<sup>11</sup>. The collapsing mechanism of the air cavity during droplet impact on hydrophobic surfaces was studied in details and it was found that the collapsing dynamics was dominated by inertia, similar to pinching-off of bubbles in liquid<sup>11</sup>. However, for larger impact velocity, inertia no longer dictates air cavity collapse that leads to very high jet velocity or bubble entrapment in the liquid bulk<sup>11,12</sup>. The reason for this transition remains elusive. Does the intervening air film have any role in dictating this transition? Most experimental studies involving droplet impact on hydrophobic surfaces utilized side-view imaging, which is incapable of resolving both the bulk cavity collapse and rupture of the air film<sup>11–13</sup>. Hence, interactions between the air film and the collapsing air cavity are largely unexplored.

To probe such interactions, a necessary condition is the air films under impacting droplets must be sustained during air cavity formation in the bulk of the droplets. This condition is rarely met for impacts on rigid hydrophilic or hydrophobic surfaces due to random air film rupture<sup>5,6,11,12</sup>. Random rupture and subsequent wetting causes premature collapse of the air cavity in the bulk. Recent experiments have shown droplets impacting soft, hydrophobic surfaces increases the lifetime of the air film<sup>14</sup>. A sustained air film trapped between the impacting droplet and the solid inhibits wetting initiation and can also facilitate higher bouncing probability<sup>15</sup>. At the same time, it enables us to probe the interactions between the air cavity in the bulk and the en-

<sup>a</sup> School of Physical & Mathematical Sciences, Nanyang Technological University, 50 Nanyang Avenue, 639798 Singapore

<sup>b</sup> School of Mechanical & Aerospace Engineering, Nanyang Technological University, 50 Nanyang Avenue, 639798 Singapore. E-mail: \* xqvo@ntu.edu.sg, \*\* ttran@ntu.edu.sg

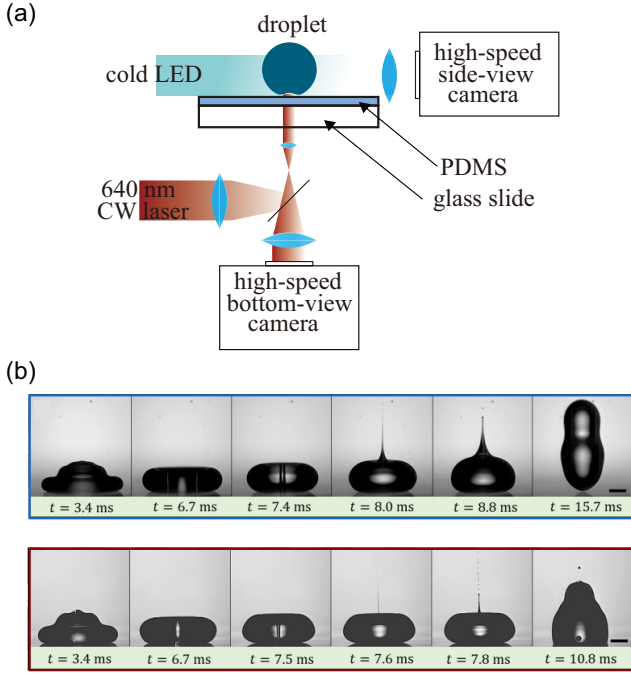


**Fig. 1** (a) Schematic of the experimental setup. (b) Impact dynamics of a 1.16 mm water droplet on soft PDMS 60:1 substrates with Young's modulus  $E = 4.8 \text{ kPa}$  and two impact velocities:  $0.33 \text{ ms}^{-1}$  ( $We = 1.7$ ) (upper panel),  $0.39 \text{ ms}^{-1}$  ( $We = 2.4$ ) (lower panel). The snapshots corresponding to the last column in both panels show two different impact outcomes: bouncing and deposition with entrapped air bubble. Scale bars represent 0.5 mm.

trapped air film beneath the drop. Further, how such interactions affect the macroscopic behaviour of the impacting liquid droplets is an interesting unresolved question.

In this work, we experimentally study the interaction of the air cavity and the trapped air film during droplet impact on soft, hydrophobic surfaces. We aim to understand how the dynamics and rupture of the air film beneath an impacting liquid droplet affects the collapsing mechanism of the air cavity in liquid bulk. We employ both high-speed laser interferometry and high-speed optical imaging to monitor and characterize the air film evolution, as well as the formation and subsequent collapse of the air cavity. We finally provide an explanation for the occurrence of high-speed jets induced by air cavity collapse and the resulting bubble entrapment.

## 2 Experiments

Our test substrates were glass slides coated with a layer of Polydimethylsiloxane (PDMS) of thickness  $70 \mu\text{m}$ . The elasticity  $E$  of the substrate was varied from  $4.8 \text{ kPa}$  to  $263.6 \text{ kPa}$  by changing the ratio of the monomer to crosslinker from 60:1 to 30:1 (Tab. 1). The equilibrium contact angle of a small water droplet on the test substrates was  $\theta_Y = 110^\circ \pm 3^\circ$ . Impact experiments were conducted using water droplets with radius  $r_0$  varying from  $0.63 \text{ mm}$  to  $1.4 \text{ mm}$ ; the velocity  $v$  of the impacting droplets was varied between  $0.30 \text{ ms}^{-1}$  and  $0.51 \text{ ms}^{-1}$ . The Weber number, defined as  $We = \rho r_0 v^2 / \gamma$ , thus varies from 2.1 to 5.1. Here,  $\rho = 1000 \text{ kg m}^{-3}$

and  $\gamma = 72 \text{ Nm}^{-1}$  respectively are the density and surface tension of water.

Impacting droplets were recorded synchronously from the bottom and the side using two high-speed cameras (SA-X2 and SA-5, Photron) operating at imaging rates from 30,000 to 100,000 frame per second. A cold LED light source was used for side view illumination, while a red diode laser (wavelength  $\lambda = 640 \text{ nm}$ ) was used to illuminate the impacted surface from below (Fig. 1a). The laser illumination coupled with a  $5\times$  optical zoom lens enabled us to observe the dimple profile with a height resolution of  $\lambda/4 = 160 \text{ nm}$ <sup>6,16</sup>, and a horizontal resolution of  $3.5 \mu\text{m}/\text{pixel}$ .

## 3 Results and Discussions

### 3.1 Dimple inversion upon droplet impact

For impacts of low viscosity liquids, the intrinsic length scale of the capillary waves induced upon impact is the wavelength  $\lambda_c \sim \gamma \rho^{-1} v^{-2}$ <sup>11</sup>. The condition for capillary wave formation is  $\lambda_c > r_0$ , or equivalently  $We > 1$ . As the Weber number in our experiment varies between 2 and 5, both inertial and capillary forces are significant. In this Weber number range, impacting droplets deform into pyramidal shapes, as shown in Fig. 1b ( $t = 3.4 \text{ ms}$ ).

From side-view images, we observe two distinct macroscopic behaviours when the velocity  $v$  of an impacting droplet increases: the droplet either bounces off from the substrate at low impact velocity (Fig. 1b, upper panel) or is deposited onto the substrate as the impact velocity is increased (Fig. 1b, lower panel). In both cases, we observe that the air cavity forms roughly at the moment the droplet reaches the maximum deformation and starts retracting (Fig. 1b,  $t = 6.7 \text{ ms}$ ). Subsequently, the air cavity collapses resulting in liquid jets from the droplet. Typically, we observe that the jet velocity is higher in the case of depositing droplets compared to that of bouncing droplets from the substrate.

To reveal mechanisms causing the different impact outcomes, i.e., bouncing or deposition, in Fig. 2, we show bottom-view interferometric recordings and the corresponding extracted profiles of the air film trapped between the liquid and the solid upon impact. In all cases, the liquid droplet initially skates on a thin film of air with the bottom liquid-air interface expanding at a lateral speed  $\sim 0.2 \text{ ms}^{-1}$ , in close proximity to those reported in a recent study for impacts in a similar range of Weber number<sup>17</sup>. While expanding, the bottom surface of the droplet deforms into the familiar dimple profile<sup>4,6</sup> with two distinct kinks due to excess pressure in the trapped air film, evident from the recorded interference signatures (see Fig. 2 a-d,  $t = 0.34 \text{ ms}$ ).

The evolution of the trapped air film is sensitive to the impact velocity. At low impact velocity,  $v \leq 0.36 \text{ ms}^{-1}$  (Fig. 2a), the air film remains intact during the entire duration of impact. There-

**Table 1** Substrates used in our experiments. The numbers show the weight ratio of the monomer to crosslinker. The value of stiffness  $E$  is measured experimentally using a rheometer.

Substrates:	P60:1	P50:1	P40:1	P35:1	P30:1
$E$ (kPa)	4.8	29.5	70.9	142.7	263.6

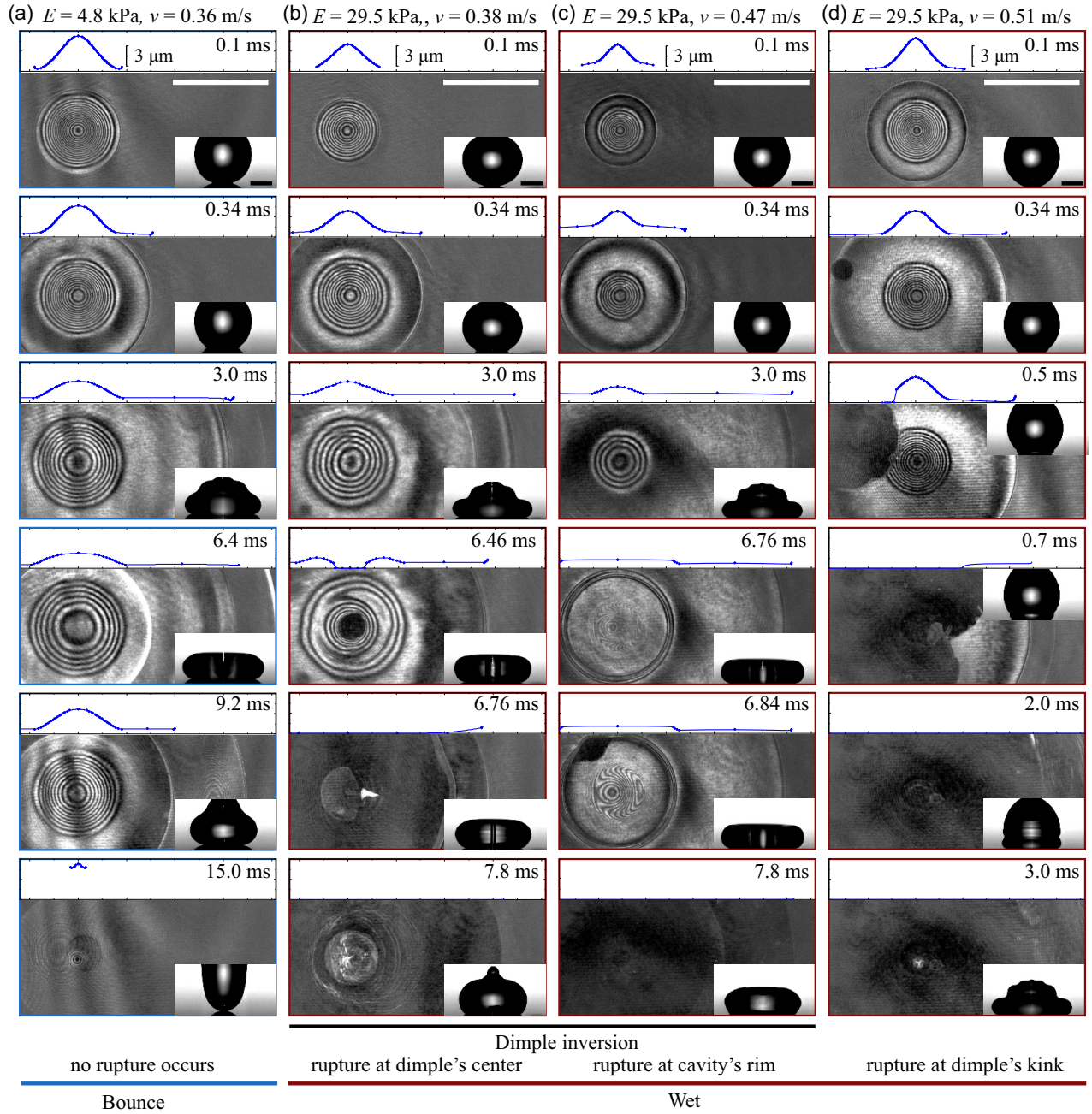


**Fig. 2** Air film rupture dynamics of 1.4 mm radius water drops impacting on soft PDMS surfaces at different impact velocity  $v$ . (a) At  $v = 0.36 \text{ ms}^{-1}$ , the droplet bounces off after impact without wetting the solid surface. (b) At  $v = 0.38 \text{ ms}^{-1}$ , a perfect inversion of the air cavity causes rupture of the air film at the dimple's center. Liquid jet and air bubble entrapment caused by the collapse of air cavity are observed. (c) At  $v = 0.47 \text{ ms}^{-1}$ , rupture of air film occurs at the rim of the air cavity. (d) At  $v = 0.51 \text{ ms}^{-1}$ , rupture of air film occurs randomly at the rim location where the air film is thinnest. The scale bars in both side-view and bottom-view images represent 1 mm.

fore, the droplet bounces off from the substrate similar to previous studies involving droplet bouncing on glass<sup>5</sup> and PDMS<sup>15</sup> surfaces. For  $0.38 \text{ ms}^{-1} \leq v \leq 0.47 \text{ ms}^{-1}$ , the air cavity in the bulk forces the dimple downward causing shape inversion. The air film separating the inverted dimple and the soft solid eventually ruptures, initiating wetting. Interestingly, we observe two distinct types of wetting initiation caused by the inversion of the dimple: wetting either first occurs at the center of the dimple (Fig. 2b,  $t = 6.76 \text{ ms}$ ) or at the dimple's rim (Fig. 2c,  $t = 6.84 \text{ ms}$ ). The

wetting initiation at the dimple's rim consistently happens at impact velocity slightly higher than that at the dimple's center. For a higher range of impact velocity,  $v \geq 0.51 \text{ ms}^{-1}$ , rupture of the air film initiates at a random position near the inner or outer kink (Fig. 2d,  $t = 0.34 \text{ ms}$ ) consistent with previous drop impact studies on rigid and soft surfaces<sup>4,6,15</sup>.

In Fig. 3, we show a phase diagram presenting how the Weber number  $We$  and surface elasticity  $E$  affect the behaviour of the trapped air film and the resulting impact outcomes. Gener-



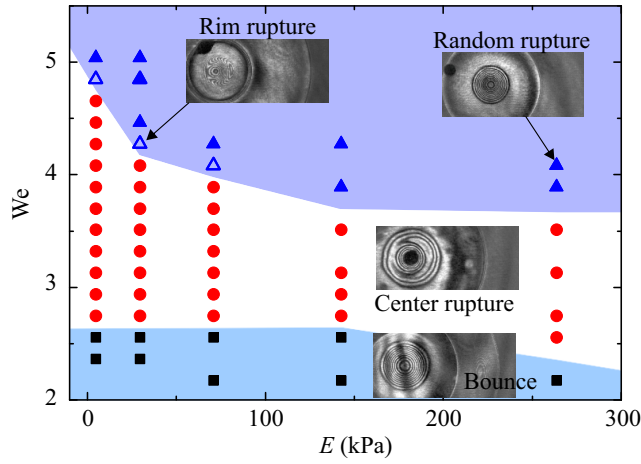


**Fig. 3** Phase diagram showing the general behaviours, i.e., bouncing, dimple inversion and wetting, of droplets impacting on soft solid. The behaviours are obtained by varying Weber number  $We$  and Young modulus  $E$  of the soft substrates. The droplet is water having fixed radii  $r_0 = 1.4$  mm.

ally, we observe that dimple inversion causing air film rupture at the center of the dimple is sandwiched between two other major behaviours: bouncing and random rupture. Wetting initiated by rupture at the dimple's rim (open triangles) appears as a transitional behaviour separating the center rupture and the random rupture behaviours. In other words, for a fixed soft substrate, increasing the  $We$  number causes the impact dynamics to change from bouncing to center rupture, rim rupture and finally random rupture. For surfaces with  $E > 142$  kPa, we do not observe the rim rupture behaviour. We also observe that increasing the substrate elasticity  $E$ , while causing insignificant effect to the transition between bouncing and wetting considerably reduces the transitional  $We$  number between center rupture and rim rupture. This is qualitatively consistent with the fact that increasing the surface stiffness results in less air entrapment and thinner air film, which eventually leads to random rupture of the air film and wetting initiation<sup>5,6</sup>.

### 3.2 Collapse dynamics of air cavity

The dimple and air film dynamics not only affect the general impact outcomes but also alter the formation and collapse of the air cavity formed upon impact. In Fig. 4, we show several series of snapshots highlighting the formation and collapse of the air cavity upon impact of  $r_0 = 1.4$  mm water droplets on soft PDMS surfaces having  $E = 70.9$  kPa. At low impact velocity, i.e.,  $v = 0.33$  ms<sup>-1</sup>, we observe that a U-shaped cavity is partially formed (Fig. 4a). Subsequently, the droplet's surface restores to its minimum surface area pushing the cavity out. No liquid jet or air bubble entrapment inside the liquid bulk is observed. At  $v \geq 0.36$  ms<sup>-1</sup>, the capillary waves on the droplet's surface are sufficiently strong to form a cylindrical cavity through the droplet width (Fig. 4b-f, the first snapshots). Subsequently the cavity radius retracts and eventually collapses resulting in liquid jet and bubble entrapment. Depending on the impact velocity  $v$ , the cavity either collapses at the

bottom of the cylindrical cavity (Fig. 4b,  $t = 7.36$  ms), or at the cavity's waist (Fig. 4c,  $t = 6.82$  ms), cavity's top (Fig. 4d,  $t = 7.16$  ms) or at both top and bottom (Fig. 4e,  $t = 7.60$  ms). We attribute the different collapsing dynamics of the cavity to the capillary waves on the cavity surface which is clearly observed in (Fig. 4b-e): the collapse position occurs at the wave's peak. At high impact velocity, where the air film ruptures randomly, (Fig. 4f), the wetting initiation at the rupture point disturbs the retracting cavity in the bulk.

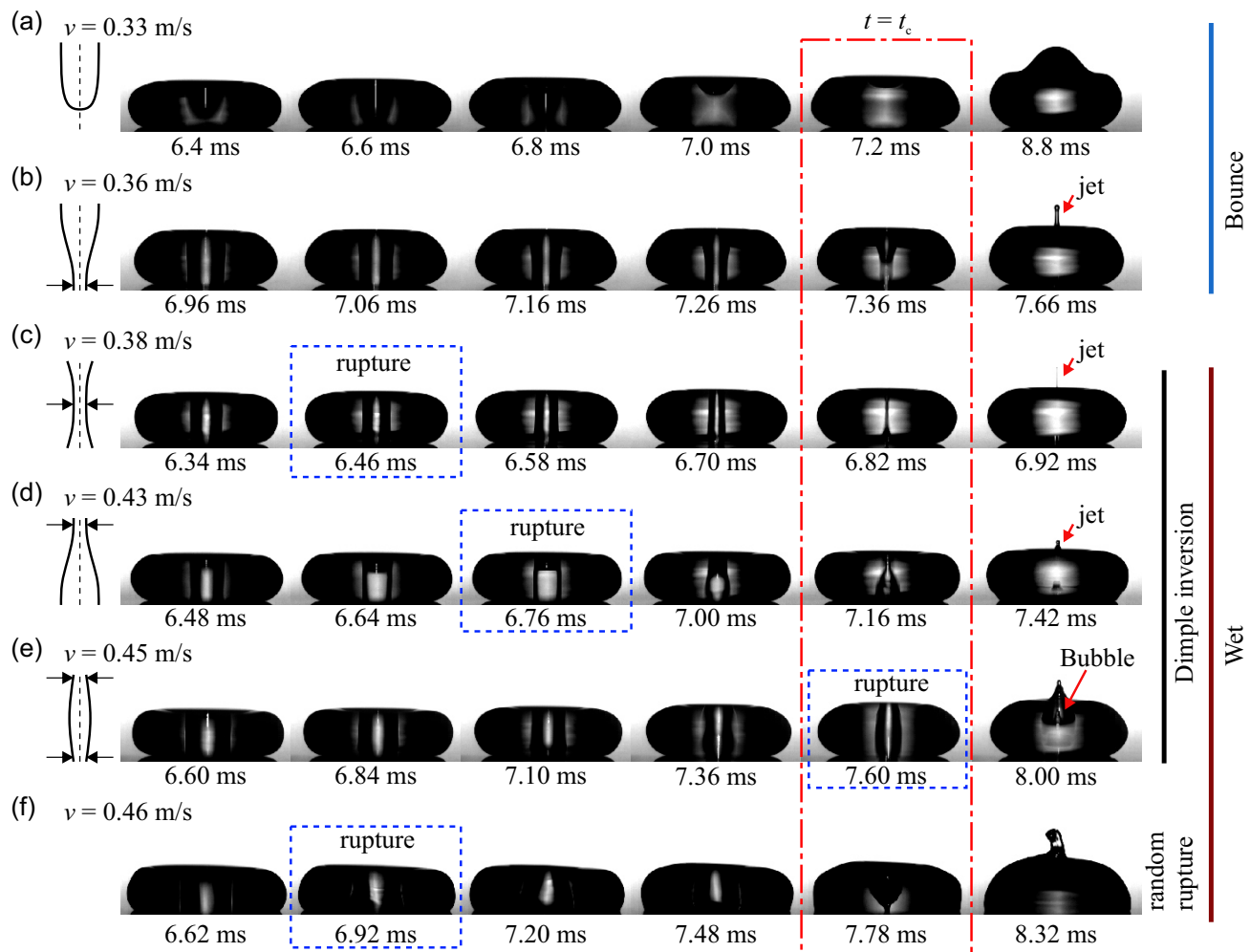
To quantitatively characterize the collapsing dynamics of the air cavity, we measure the evolution of the retracting cavity radius  $r_c$ . In Fig. 5, we show the dependence of  $r_c$  on  $t_c - t$  for different impact outcomes, i.e., bounce or wet, while varying the surface elasticity  $E$ , droplet radius  $r_0$ , and impact velocity  $v$ . Here,  $r_c$  is the cavity radius measured along the location where the air cavity eventually collapses,  $t_c$  the time instant when the retracting cavity completely collapses. It should be noted here that we only show values of  $r_c$  measured in the case that the air cavity symmetrically collapses, which case occurs when the droplets bounces or wet the substrate by dimple inversion (Fig. 4b-e). In the case that random rupture occurs, it is not possible to accurately measure  $r_c$  as the cavity collapses asymmetrically (Fig. 4f). We observe two distinct collapsing behaviours depending on the impact outcomes:  $r_c \sim (t_c - t)^{1/2}$  for bouncing droplets (Fig. 5a,b), and  $r_c \sim (t_c - t)^{2/3}$  for wetting induced by dimple inversion (Fig. 5c,d). Surprisingly, elasticity of the substrate  $E$  does not affect the dependence of  $r_c$  on  $t_c - t$  in both bouncing and dimple inversion regimes. In other words, although surface elasticity significantly affects the transition between bouncing and dimple inversion, the formation and collapse of the air cavity is mainly determined by the hydrodynamical properties of the droplets.

For impacts in the bouncing regime (Figs. 2a and 4a,b), it was shown in previous studies<sup>11,12,18</sup> that the air cavity's dynamics is dominated by inertia, leading to the relation  $r_c \sim (\gamma r_0)^{1/4} \rho^{-1/4} (t_c - t)^{1/2}$ . This is indeed consistent with the power law  $r_c \sim A(t_c - t)^{1/2}$  observed in our experiment (Fig. 5a,b). Fitting this power law to our experimental data collected for  $r_0$  in the range from 0.63 mm to 1.4 mm respectively yields  $A$  from 0.010 to 0.022 consistent with the calculated values of  $(\gamma r_0)^{1/4} \rho^{-1/4}$  from 0.014 to 0.020.

For impacts in which the air film ruptures due to dimple inversion, we observe a different power-law behaviour for the collapsing cavity radius. We argue that the fast contact line motion at the rupture point generates capillary waves on the cavity's surface (Fig. 4); these waves act as the driving factor for the subsequent collapse of the cavity. As the collapsing dynamics is in the inertial regime, the capillary waves are self-similar with phase velocity  $v \sim \gamma^{1/3} [\rho(t_c - t)]^{-1/3}$ <sup>19-22</sup> in the present context. Consequently, balancing the dynamical pressure  $\rho v^2$  with the Laplace pressure  $\gamma r_c^{-1}$  at the collapsing position results in an expression for retracting cavity radius:

$$r_c \sim \left( \frac{\gamma}{\rho} \right)^{1/3} (t_c - t)^{2/3}. \quad (1)$$

Eq. 1 indicates that the dependence of  $r_c$  on  $t_c - t$  in the case that



simple inversion happens does not depend on either droplet radius  $r_0$  or the impact velocity  $v$ , consistent with our experimental data shown in Fig. 5d.

When the air cavity collapses due to necking, it is divided into two air cavities which subsequently evolve differently under surface tension effects. On one hand, the enclosed geometry of the lower air cavity prevents the air from escaping and eventually results in an air bubble entrapped inside the liquid bulk. On the other hand, the upper air cavity, which is connected to the ambient air at its top continues to collapse and finally generates a liquid jet as illustrated in Fig. 1b. As a result, the jetting dynamics, i.e., the jet's radius and velocity, strongly depends on the collapsing dynamics of the air cavity.

(Fig. 4c) or conical cavity (Fig. 4b,d). When jetting is induced by cylindrical air cavity collapse, we observe that the jets have small radius and high velocity (Fig. 6a). The jet's shape does not depend on whether the droplets bounce or wet the solid. However, we observe that the jetting velocity is much higher when the droplets wet the solid by dimple inversion compared to that when it bounces. For wetting by dimple inversion, we observe jet velocity as high as  $37\text{ ms}^{-1}$ . Whereas, for bouncing scenarios, the jet velocity observed is typically in the range  $2\text{ ms}^{-1} - 10\text{ ms}^{-1}$ . When the air cavity collapses at its ends, the so-called conical collapse (Fig. 6b), the jets have larger radius and lower velocity compared to those of the cylindrical collapse. Typical jet velocity for conical collapse is approximately  $2\text{ m.s}^{-1}$ . Whether the air film ruptures or not does not significantly affect either the radius or velocity of the jets.

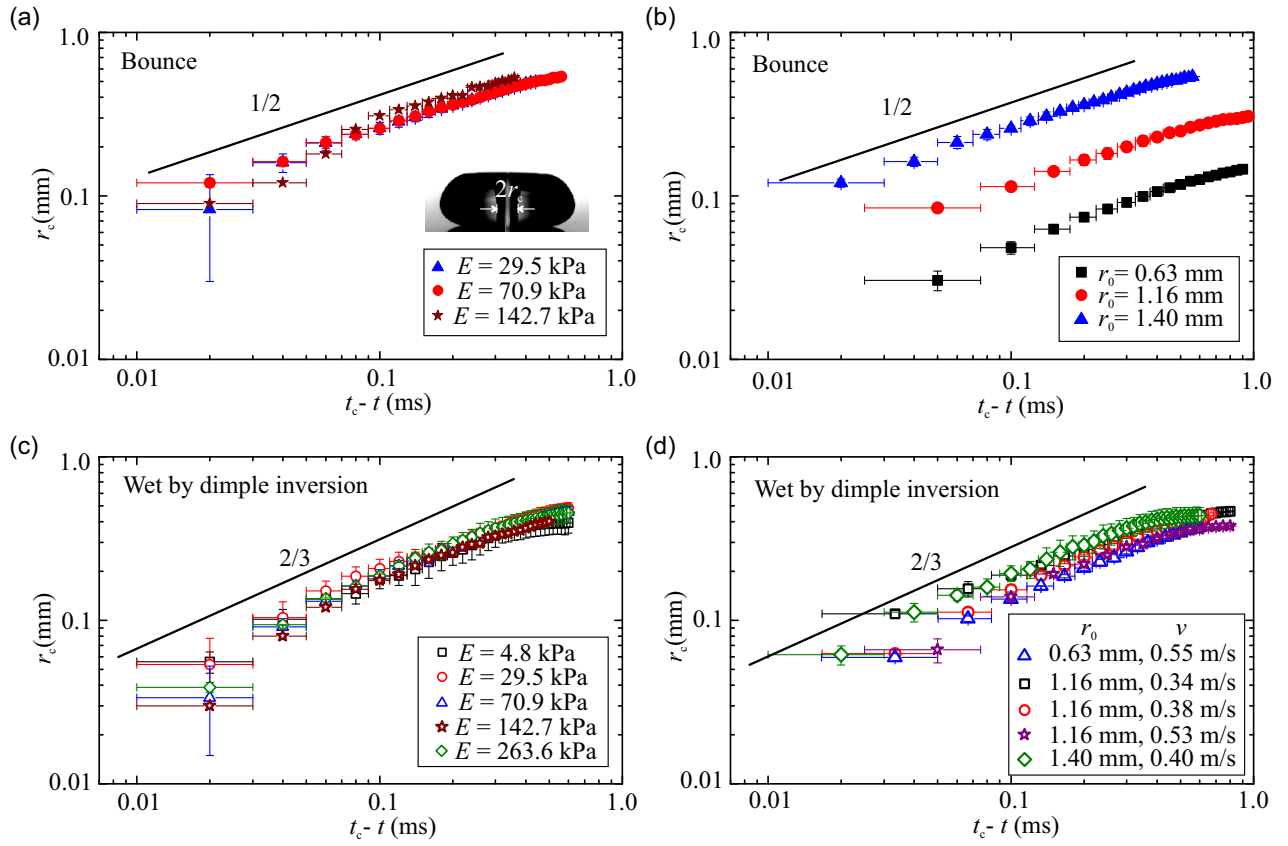


**Fig. 5** (Color online) Plots showing the dependence of air cavity radius  $r_c$  with  $t_c - t$  for different impact outcomes, i.e., bounce or wet, and different experimental parameters: (a) droplets bounce,  $r_0 = 1.4$  mm,  $v = 0.36$  ms $^{-1}$ , varying  $E$ ; (b) droplets bounce,  $E = 4.6$  kPa,  $We \approx 2$ , varying  $r_0$ ; (c) droplets wet the solid by dimple inversion,  $r_0 = 1.4$  mm,  $v = 0.39$  ms $^{-1}$ , varying  $E$ ; (d) droplet wet the solid by dimple inversion,  $E = 4.6$  kPa, varying both  $r_0$  and impact velocity  $v$ .

entrapped air bubble freely floats around in the liquid bulk. Contrary to liquid impact on rigid surfaces<sup>23</sup>, we do not observe any sessile air bubble pinned to the surface.

### 3.3.2 Jets induced by dimple burst

For surfaces with  $E < 70.9$  kPa and impact velocity  $v \approx 0.45$  m.s $^{-1}$ , we witness a special case of impact outcome: upon dimple inversion, a thin liquid jet emanates from the bottom of the retracting air cavity and shoots upwards (see Fig. 6c). This jetting behaviour is caused by rupture of the thin liquid film separating the retracting air cavity and inverted dimple. Typically, the jet radius varies between 15  $\mu$ m and 45  $\mu$ m. It appears that the liquid jet expands radially briefly, for a duration of 60  $\mu$ s - 80  $\mu$ s, before terminating into tiny droplets. The liquid jetting is immediately followed by air cavity collapse and its accompanying jet. Hence, for such impact scenarios, we observe jets from both thin liquid film collapse and air cavity collapse, a phenomenon previously not witnessed.

## 4 Concluding remarks

In summary, we have experimentally investigated the interaction between the collapsing air cavity in the bulk of an impacting droplet and the air film separating the droplet with the impacted soft surface. Above a threshold impact velocity, the interaction induces inversion of the dimple in the air film and subsequently

ruptures the air film. This behaviour is in a stark contrast to random air film rupture commonly witnessed<sup>6,14</sup>. The air film rupture in return dictates the final collapsing mechanism of the air cavity. The rupture pins the base of the retracting bulk cavity to the surface and influences its collapsing dynamics. In contrast to unperturbed collapse of an air cavity, cavity collapse is influenced by capillary waves generated upon pinning leading to various possible locations of collapse. The collapsing radius exhibits self-similarity and obeys a 2/3 power-law in time. The observed collapsing behaviour is reminiscent of inertia-capillary break-away of a tapered fluid sheet<sup>24</sup> and other self-similar phenomena observed in free surface flows. For such collapsing mechanism, we further observe that the lower half of the collapsed air cavity causes entrapment and formation of an air bubble, while the upper half induces a liquid jet with velocity which can be as high as 100 folds of the impact velocity.

We highlight that within the tested velocity range, dimple inversion and its subsequent rupture causes wetting initiation at the center, as opposed to random rupture locations<sup>6,14</sup>. This mode of liquid-solid contact is a more controlled event where the liquid-solid footprint radius expands in a radially symmetric manner, similar to onset of quasi-static spreading of liquid drops on surfaces<sup>25,26</sup>. Furthermore, we observe a transition from droplet bouncing accompanied with  $t^{1/2}$  cavity collapse to dimple inver-

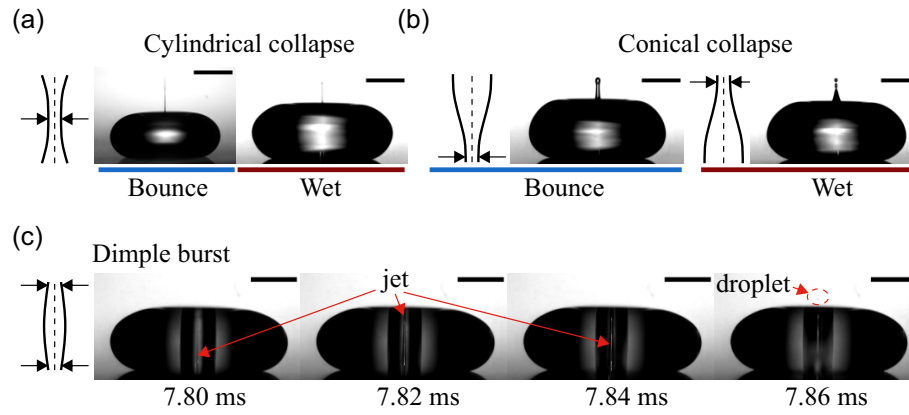


**Fig. 6** (a) Snapshots showing the jetting dynamics by air cavity collapsing at its waist. Parameters: for the left snapshot (bounce),  $E = 4.8 \text{ kPa}$ ,  $v = 0.34 \text{ ms}^{-1}$ ,  $r_0 = 1.16 \text{ mm}$ ; for the right snapshot (wet),  $E = 70.9 \text{ kPa}$ ,  $v = 0.38 \text{ ms}^{-1}$ ,  $r_0 = 1.4 \text{ mm}$ . (b) Snapshots showing the jetting dynamics by air cavity collapsing at its ends, i.e., bottom end, top end or both. Parameters: for the left snapshot (bounce),  $E = 70.9 \text{ kPa}$ ,  $v = 0.36 \text{ ms}^{-1}$ ,  $r_0 = 1.4 \text{ mm}$ ; for the right snapshot (wet)  $E = 29.5 \text{ kPa}$ ,  $v = 0.45 \text{ ms}^{-1}$ ,  $r_0 = 1.4 \text{ mm}$ ; (c) Snapshots showing the jetting dynamics by dimple burst upon inversion of the dimple. Parameters:  $E = 4.8 \text{ kPa}$ ,  $v = 0.47 \text{ ms}^{-1}$ ,  $r_0 = 1.4 \text{ mm}$ . In all cases, the scale bars represent 1 mm.

sion induced wetting initiation accompanied with  $t^{2/3}$  cavity collapse at  $We \approx 2$ . The physical significance of this transition and the influence of surface wettability remain open questions for future studies.

## Conflicts of interest

There are no conflicts to declare.

## Acknowledgments

The authors thank Maurice H. W. Hendrix for valuable discussions regarding the procedure to extract dimple profile shape from interference fringes. This study is supported by Nanyang Technological University (NTU) and A\*STAR (SERC Grant No. 1523700102). S.M. is supported by NTU Research Scholarship.

## Notes and references

- 1 M. M. Driscoll and S. R. Nagel, *Phys. Rev. Lett.*, 2011, **107**, 154502.
- 2 N. Ashgriz, *Handbook of Atomization and Sprays: Theory and Applications*, Springer Science & Business Media, 2011.
- 3 J. M. Kolinski, S. M. Rubinstein, S. Mandre, M. P. Brenner, D. A. Weitz and L. Mahadevan, *Phys. Rev. Lett.*, 2012, **108**, 074503.
- 4 J. de Ruiter, J. M. Oh, D. van den Ende and F. Mugele, *Phys. Rev. Lett.*, 2012, **108**, 074505.
- 5 J. de Ruiter, R. Lagraauw, D. van den Ende and F. Mugele, *Nat. Phys.*, 2015, **11**, 48.
- 6 J. de Ruiter, D. van den Ende and F. Mugele, *Phys. Fluids*, 2015, **27**, 012105.
- 7 R. C. van der Veen, T. Tran, D. Lohse and C. Sun, *Phys. Rev. E*, 2012, **85**, 026315.
- 8 B. Bhushan and Y. C. Jung, *Prog. Mater. Sci.*, 2011, **56**, 1–108.
- 9 E. Li and S. T. Thoroddsen, *J. Fluid Mech.*, 2015, **780**, 636–648.
- 10 E. Klaseboer, R. Manica and D. Y. Chan, *Phys. Rev. Lett.*, 2014, **113**, 194501.

- 11 D. Bartolo, C. Josserand and D. Bonn, *Phys. Rev. Lett.*, 2006, **96**, 124501.
- 12 L. Chen, L. Li, Z. Li and K. Zhang, *Langmuir*, 2017, **33**, 7225–7230.
- 13 D. Richard, C. Clanet and D. Quéré, *Nature*, 2002, **417**, 811–811.
- 14 K. Langley, A. A. Castrejon-Pita and S. T. Thoroddsen, *Soft Matter*, 2020.
- 15 L. Chen, E. Bonaccorso, P. Deng and H. Zhang, *Phys. Rev. E*, 2016, **94**, 063117.
- 16 M. H. Hendrix, R. Manica, E. Klaseboer, D. Y. Chan and C.-D. Ohl, *Phys. Rev. Lett.*, 2012, **108**, 247803.
- 17 M. Y. Pack, A. Yang, A. Perazzo, B. Qin and H. A. Stone, *Phys. Rev. Fluids*, 2019, **4**, 123603.
- 18 M. S. Plesset and A. Prosperetti, *Annu. Rev. Fluid Mech.*, 1977, **9**, 145–185.
- 19 R. F. Day, E. J. Hinch and J. R. Lister, *Phys. Rev. Lett.*, 1998, **80**, 704.
- 20 D. Leppinen and J. R. Lister, *Phys. Fluids*, 2003, **15**, 568–578.
- 21 R. Cox, *J. Fluid Mech.*, 1986, **168**, 169–194.
- 22 Q. Vo and T. Tran, *arXiv preprint arXiv:2101.02821*, 2021.
- 23 W. Bouwhuis, R. C. van der Veen, T. Tran, D. L. Keij, K. G. Winkels, I. R. Peters, D. van der Meer, C. Sun, J. H. Snoeijer and D. Lohse, *Phys. Rev. Lett.*, 2012, **109**, 264501.
- 24 J. B. Keller and M. J. Miksis, *SIAM J. Appl. Math.*, 1983, **43**, 268–277.
- 25 A.-L. Biance, C. Clanet and D. Quéré, *Phys. Rev. E*, 2004, **69**, 016301.
- 26 S. Mitra and S. K. Mitra, *Langmuir*, 2016, **32**, 8843–8848.